Rotation Curve Measurement using Cross-Correlation [1]

Elizabeth J. Barton[2], Sheila J. Kannappan, Michael J. Kurtz, Margaret J. Geller
Harvard-Smithsonian Center for Astrophysics

ABSTRACT

Longslit spectroscopy is entering an era of increased spatial and spectral resolution and increased sample size. Improved instruments reveal complex velocity structure that cannot be described with a one-dimensional rotation curve, yet samples are too numerous to examine each galaxy in detail. Therefore, one goal of rotation curve measurement techniques is to flag cases in which the kinematic structure of the galaxy is more complex than a single-valued curve.

We examine cross-correlation as a technique that is easily automated and works for low signal-to-noise spectra. We show that the technique yields well-defined errors which increase when the simple spectral model (template) is a poor match to the data, flagging those cases for later inspection.

We compare the technique to the more traditional, parametric technique of simultaneous emission line fitting. When the line profile at a single slit position is non-Gaussian, the techniques disagree. For our model spectra with two well-separated velocity components, assigned velocities from the two techniques differ by up to $\sim$52% of the velocity separation of the model components. However, careful use of the error statistics for either technique allows one to flag these non-Gaussian spectra.

Subject headings: methods: data analysis — techniques: radial velocities

1. Introduction

Spatially resolved optical spectroscopy became a tool for studying the dynamics of external galaxies when Pease (1918) observed rotation in the inner part of M31 (Rubin 1995). Later, Babcock (1939) effectively measured an optical "rotation curve" of M31 by measuring velocities of individual nebular regions separately. Although required exposure times were very long, somewhat larger samples of rotation curves were amassed in the inner portions of galaxies (Burbidge &

[1] Observations reported in this paper were obtained at the Multiple Mirror Telescope Observatory, a facility operated jointly by the University of Arizona and the Smithsonian Institution.

[2]present address: National Research Council of Canada, Herzberg Institute of Astrophysics, Dominion Astrophysical Observatory, 5071 W. Saanich Road, RR5, Victoria, BC, Canada V8X 4M6

Burbidge 1975), and finally in the outer regions. Now, optical rotation curves of nearby galaxies can be measured with brief exposure times, enabling the construction of very large samples of rotation curves for statistical purposes (e.g. Rubin et al. 1985; Mathewson, Ford & Buchhorn 1992; Courteau 1997).

Improvements in the spatial and velocity resolution of optical spectrographs have revealed complex velocity structure in both elliptical and spiral galaxies. The phenomena include distinct, nuclear kinematic components in spiral galaxies (e.g. Marziani et al. 1994; Rubin, Kenney & Young 1997; Bureau & Freeman 1999), and in the cores of elliptical galaxies (e.g. Franx, Illingworth & Heckman 1989).

The physics behind the complex velocity structure seen in emission lines is difficult to unravel. Although there are numerous techniques for inferring the line-of-sight velocity structure of a stellar system from a non-Gaussian *absorption* line profile (e.g. Rix & White 1992; van der Marel & Franx 1993; Merrifield & Kuijken 1994), the analogous measurements for emission-line kinematics are largely unconstrained. Emitting regions have non-uniform internal velocity structure which complicates the structure of the emission lines (e.g. from individual HII regions; Osterbrock 1989).

To date, estimates of the true kinematic structure of galaxies with complex emission line profiles are largely qualitative (e.g. Rubin et al. 1997), and most rotation curve reductions assign a single velocity at each slit position. In most longslit, emission-line spectroscopic studies, velocities are computed with some form of Gaussian line fitting (e.g. Keel 1996) or line centroiding or peak fitting (e.g. Courteau 1997; Rubin et al. 1997), of either the brightest emission line or a subset of emission lines simultaneously. Mathewson et al. (1992) and Márquez & Moles (1996) use cross-correlation to measure rotation curves, but without detailed description of their technique.

In this era of large, high-quality rotation curve samples, techniques for rotation curve reduction need to be re-examined. Here, we evaluate a little-used but easily-implemented technique for longslit rotation curve reduction, cross correlation. We give special attention to the fact that each aperture along the slit may contain emission from multiple velocities. The technique (1) yields a well-defined response to all line profiles — the velocity and error have a clear physical relationship to the observed line profile, (2) is accurate when extracting redshifts of low signal-to-noise (S/N) spectra, and (3) is easily automated. Focusing on (1), we compare the technique to the fundamentally different, parametric technique of Gaussian line fitting.

We test the techniques for redshift measurement in a controlled manner, using model spectra with varied properties. Our intent is to highlight the most relevant features of the techniques, not to explore parameter space exhaustively. In § 2, we describe two techniques which represent fundamentally different approaches, cross-correlation and Gaussian fitting. In § 3, we test them with single-aperture Gaussian and two-component line profiles, to illustrate that when the line profile is non-Gaussian, different techniques can yield different results, and to track the error behavior. In § 4, we apply the techniques to two-dimensional model rotation curves to illustrate the error behavior in situations which commonly arise in longslit spectroscopy. In § 5 we briefly discuss applying cross-correlation to longslit spectral data. We conclude in § 6.

2. Exploring Cross-Correlation and Simultaneous Emission Line Fitting

We evaluate an effective technique for redshift measurement, cross-correlation (XC), which is little-used for emission-line measurements. We compare it to an alternative technique, simultaneous emission line fitting (SEMLF; as in Keel 1996). The techniques represent the two fundamentally different approaches to these measurements. SEMLF is parametric, involving modeling the emission lines and fitting for the parameters. XC is non-parametric in the sense that we do not fit for parameters, although the technique does involve assumptions — we use a model spectrum for a template in the computation. Our comparison of the techniques shows that when a single-velocity measurement is ill-defined, as when components at two separate velocities contribute to the spectrum, different approaches yield different results. Thus, these cases must be flagged and dealt with separately for a proper characterization of the velocity structure of each galaxy.

Both techniques can be reliably automated, although SEMLF requires some fine-tuning, as does XC in the low S/N case. XC is easily implemented with **xcsao** (see Kurtz & Mink 1998), within the IRAF (Tody 1986; 1993) environment. We use a version of SEMLF based on that of Kannappan et al. (1999) implemented with IDL (Landsman 1995). Both techniques apply a specific model to the data — they assume a pre-determined line profile which is usually a Gaussian. However, longslit observations are designed to detect spatially separated components *at different velocities*. These components may broaden line profiles, or may turn them into double-peaked profiles. When the Gaussian model is not a good representation of the data, the techniques will produce different results. Below, we explore results for Gaussian and double-Gaussian profiles.

We use artificial emission-line spectra with noise to explore and compare the XC and SEMLF techniques. We construct the spectra with the **linespec** task in RVSAO, and add noise with **mknoise** in NOAO.ARTDATA. Figure 1 shows the basic spectrum, a set of 5 Gaussian profiles centered at the major emission lines, Hα, [SII] and [NII], redshifted to 4000.0 km s^{-1}. We choose linewidths typical of spectra taken with a 1200 g/mm grating and a narrow (1.0$''$) slit — Hα has a full width at half maximum (FWHM) of 2.3 Å = 104 km s^{-1}. The other lines satisfy $2.26 \leq \mathrm{FWHM} \leq 2.50$ Å. To add the noise, we assume a gain of 1.5 e$^-$/DN and a read noise of 7.0 e$^-$. Although the continuum S/N ratio is not defined in these model spectra, the effective signal-to-noise ratio of the Hα line is very large in many of them: the Hα signal in the spectrum in Fig. 1 is $\sim$2300 e$^-$ over 5 pixels, so the S/N ratio in Hα is $\sim$45. Although we vary the S/N ratio in the model spectra in the examples of § 3.1, most of the other test spectra have comparably large S/N ratios. The discrete pixel sampling scale is $\sim$22 km s^{-1}.

2.1. The Cross-Correlation Technique

Kurtz & Mink (1998) describe cross-correlation exhaustively for application to redshift surveys, using the task **xcsao** in the RVSAO package, within the IRAF environment (Tody 1986, 1993). They include template construction and error analysis in their discussion. We apply the XC technique using **xcsao** in RVSAO, according to the procedure that would be used for actual data (excluding bias subtraction, flat-fielding, wavelength calibration, and cosmic ray removal). We construct the template based on the median widths and relative heights of the "emission lines" in a large ensemble of model spectra, just as we would for actual data (see § 4). Because the high-resolution models are undersampled relative to the optimal sampling rate for **xcsao**, we must adjust the rebinning in **xcsao**, by using both linear and spline3 interpolation and choosing the best result based on the r statistic.

Fig. 2 shows a sample peak in the correlation function, which **xcsao** fits to find the velocity for the spectrum in Fig. 1. Because the sample spectrum has a very large S/N ratio and a nearly-perfect Gaussian profile, the peak is well-defined and the redshift, 4001.1 ± 0.4 km s^{-1}, is close to the input model value of 4000 km s^{-1}.

Cross-correlation errors include the effects of spectrum/template mismatch, and therefore have a clear relationship to the spectral profile. The internal error estimator of Kurtz & Mink (1998) follows from the discussion in Tonry & Davis (1979, TD hereafter), with the additional assumption that the noise is sinusoidal. **xcsao** computes an error of $\frac{3}{8}\frac{\omega}{1+r}$, where ω is the FWHM of the correlation peak and r, defined by TD, is a measure of the noise based on the antisymmetric part of the correlation function. TD assume that the (symmetric) template, convolved with a simple symmetric function, is a noise-free spectral match to the object — that all spectrum/template mismatch is the result of noise. Under these assumptions, the antisymmetric part of the correlation function yields a measure of the height of the average noise peak — a galaxy with symmetric line profiles, cross-correlated with a template with symmetric line profiles, has noise and no signal in the antisymmetric part of its correlation function. Thus, the error that **xcsao** computes is the shift in the correlation peak center that would result from a spurious noise peak, where $\frac{3}{8}\omega$ is the average distance to the nearest noise peak and, with the assumptions of TD, r is an estimate of the height of the true correlation peak divided by of the height of the average noise peak.

If r is small, there are spurious peaks in the correlation function comparable to or exceeding the highest peak. **xcsao** is likely to fit one of these spurious peaks instead of the true peak; then the computed velocity is arbitrarily far from the true velocity, much farther than the formal error indicates. Thus, r is a measure of the reliability of the redshift. Kurtz & Mink (1998) require $r > 3.0$ for automatic acceptance of the extracted redshift. However, redshifts with $r < 3.0$ can be used in longslit reduction because there are data in neighboring apertures. If **xcsao** fits the wrong peak, the redshift will appear discrepant from neighboring apertures and the reduction can be checked manually, or rejected.

If the template has a single velocity component, the assumptions underlying the error estimator are incorrect for spectra with multiple components at different velocities. In this multiple-component case, spectrum/template mismatch results from noise *and* from additional peaks in the spectrum at different velocities. The mismatch generally appears in the antisymmetric part of the correlation function, and r *measures this template mismatch.* Thus r becomes a measure of how well the template fits the spectrum. Low r values indicate a poor fit, and result in large error. ω also reflects additional nearby velocity components; an additional nearby component results in a wider correlation peak, a larger ω and a larger error. Therefore, additional velocity components enlarge XC errors significantly. Below, we explore this effect using model spectra.

Kurtz & Mink (1998) find that $\frac{3}{8}\frac{\omega}{1+r}$ systemically over or underestimates nuclear redshift errors by $\sim$20 %. For large redshift surveys consisting of nuclear spectra reduced uniformly with a single template, ω remains roughly constant. In that case, error calibration can be applied to eliminate the discrepancy. Kurtz & Mink (1998) solve for a template-dependent constant, k, where the true error is then $\frac{k}{1+r}$.

However, in longslit spectroscopy, where multiple-velocity spectra abound, ω is not constant. Throughout this paper, we use $\frac{3}{8}\frac{\omega}{1+r}$ to estimate XC errors. We recommend computing errors proportional to $\frac{\omega}{1+r}$ for all longslit reduction implemented with XC, because ω reflects the presence of multiple velocity components and wide velocity components.

2.2. The SEMLF Technique

The major steps involved in SEMLF reduction are similar to the steps required to implement cross-correlation, except that we measure velocities by fitting single-Gaussian functions to the major emission lines simultaneously, when the lines are detected at $\geq 3\sigma$. All spectra reduced with the SEMLF program were first transformed to $\log(\lambda)$ space using the task **transform** in the LONGSLIT package of IRAF, with an artificial calibration lamp image. In our implementation of SEMLF, the relative wavelengths are fixed and the linewidths are constrained to be the same value for each line; the overall linewidth and each individual peak height may vary. We derive the formal model-dependent errors from χ^2-minimization fitting using the Gaussian model (Press et al. 1992).

When the minimal $\chi^2 \neq N \pm \sqrt{N}$, where N is the number of degrees of freedom in the fit, the formal errors cannot be justified rigorously. Press et al. (1992) emphasize that these errors are unsuitable when a model is an incorrect representation of the data. Finding the true errors requires other methods (e.g. Monte Carlo simulation) which are usually computationally expensive. Authors generally compute errors that account for photon statistics; some error calculations are independent of profile shape (Courteau 1997 uses the weighted mean) and/or include line widths (Keel 1996). However, these errors do not include mismatch between the data and a basic model that in every case assumes a single, well-defined velocity. Here, we attempt to partially account for this mismatch, taking an approach guided by the analogy between XC errors and the error derived from weighting by the reduced χ^2, because χ^2 is an estimator of the suitability of the Gaussian model and reflects irregular line profiles. Although the procedure is not rigorously justified, we consider weighted errors as a computationally convenient way of achieving an estimate of the proper error behavior; below, we multiply the error by the reduced $\hat{\chi}^2 = \chi^2/N$. We demonstrate that the weighted errors display the expected error behavior and are similar to the XC errors. This similarity arises because both the XC $\frac{1}{1+r}$ statistic and the SEMLF $\hat{\chi}^2$ are based on the cross product of the object and model spectra divided by an estimator of the variance. The formal SEMLF error performs the same function as the width factor ($\frac{3}{8}\omega$) in **xcsao**; it provides a scale by which to multiply the goodness of fit measure ($\hat{\chi}^2$ for SEMLF, $\frac{1}{1+r}$ for XC) in order to estimate the uncertainty of the measurement.

The 3σ cutoff of SEMLF is analogous to imposing a lower limit on r in the XC technique. The limit is somewhat arbitrary and could be modified. In general, we do not modify the limit in our tests, so these tests do not directly compare the effectiveness of the two techniques on very low S/N spectra.

We apply the SEMLF technique to the spectrum of Fig. 1, with a redshift of 4000 km s^{-1}. The resulting fit, with a velocity and weighted error of 4000.9 ± 0.5 km s^{-1}, is nearly indistinguishable from the spectrum. Thus, both SEMLF and XC find the correct velocity of the line profiles when they are Gaussian (with large S/N ratios). SEMLF measures the proper error in the Gaussian case; thus SEMLF, used with calibration spectra consisting of Gaussian line profiles, provides one method of calibrating the XC error when necessary.

3. Behavior of the Two Techniques for One-Dimensional Spectra

In the following sections, we explore the behavior of XC and SEMLF. We use one-dimensional spectra with varying line profiles. We fix the emission line ratios to standard HII region values similar to the XC template. Later, we consider two-dimensional spectra which mimic different features of galaxy rotation curves, including varying emission-line ratios. All models match the resolution of the data described in § 3. However, most of the model spectra have larger SNR's, and therefore much larger r values, than typical rotation curve data.

3.1. Gaussian Line Profiles

We apply XC and SEMLF to a set of 400 single-Gaussian spectra identical to Fig. 1, except that Hα S/N ratios vary from $\sim$54 to < 1. XC finds a velocity with $r \geq 1.5$ for 297 of the spectra; SEMLF finds a redshift for 285 using the 3σ cutoff; we use the 283 spectra with results from both techniques for our analysis. Fig. 3a shows a histogram of the difference between the XC velocity and the input model velocity (solid line), superimposed on the difference between the SEMLF velocity and the model velocity (dashed line) for these 283 spectra. The two distributions are similar. Fig. 3b shows the same quantity divided by the error for each velocity measurement; the dotted line reflects $\hat{\chi}^2$-weighted SEMLF errors; the graph is very similar with unweighted errors. If errors were Gaussian and were properly estimated, the histograms would be Gaussian with $\sigma = 1$ (shown as the thick dot-dashed line). The results of the two techniques differ little in the case of simple, Gaussian line profiles.

These results appear to conflict with those of Kurtz & Mink (1998), who find that cross-correlation is more sensitive than emission line fitting — **xcsao** found reliable velocities for many test spectra which could not be fit with **emsao**, the automatic emission line fitting routine in RVSAO. However, the line fitting algorithm in **emsao** differs substantially from the SEMLF technique of this paper — we apply constraints to the model we fit, namely the relative wavelengths and widths of the emission lines, thus enabling the fitting of spectra with lower S/N. Therefore, velocities for low S/N spectra should be computed with techniques that assume these or similar constraints.

3.2. Double-Gaussian Line Profiles

A single, unresolved velocity component with a symmetric line profile usually dominates a wide-aperture nuclear spectrum of a galaxy; thus techniques that assign a single, systemic velocity based on the center of a galaxy are appropriate. However, longslit observations are designed to detect spatially separated components *at different velocities*. If components at distinct velocities within the same seeing disk are separated by a small velocity difference and are smoothly varying, they may only broaden the line profile. One example is the unresolved but rapidly rotating inner region of a galaxy with a circumnuclear gas disk. However, if components are separated by a large velocity they produce a multi-peaked line profile. Examples include the transition region between a rapidly rotating circumnuclear gas disk or a bar and the outer regions of a galactic disk (Rubin et al. 1997). In this case, the spectrum shows two distinct velocity components.

When line profiles are non-Gaussian, XC may yield a different velocity than either SEMLF or centroiding techniques. Because the goal of these reduction techniques is to assign a single velocity to a spectrum, none of the techniques used for rotation curve reduction, including cross-correlation, completely model the system in the multiple-component case. At best, an automated technique can reflect the presence of more than one component in the computed error statistics.

To examine the behavior of the reduction methods in the two-component case, we construct spectra equivalent to Fig. 1, except that they have two distinct Gaussian velocity components. Figs. 4 – 5 show spectra where the intensity ratios of the two velocity components are 2:1 (Fig. 4) or 4:1 (Fig. 5). In each case, the left part of the figure shows components separated by $\Delta V = 60$ km s^{-1}, or 0.58 of the FWHM of the Hα line (104 km s^{-1}), and the right side shows components separated by $\Delta V = 160$ km s^{-1}, or 1.5 times the FWHM of Hα. The figures show the "spectrum" around Hα (solid line) and the SEMLF fit (long-dashed line), along with the output XC (dashed vertical line) and SEMLF (dotted vertical line) velocities. Note that when the velocity resolution differs from the model spectra we present (the FWHM of Hα is 104 km s^{-1}), ΔV must be scaled to compare with our results.

In Fig. 4a, the two separate components are not visible as separate peaks. SEMLF and XC yield very similar results. In Fig. 4b, ΔV = 160 km s^{-1} — two distinct peaks are visible. The SEMLF technique fits one wide Gaussian to the two components. In contrast, XC finds a velocity closer to the stronger peak. The XC error increases by a factor of ~16 over the result in Fig. 4a, signaling the presence of the two distinct components. Appropriately, r decreases substantially, from 192 to 14, and and ω increases from 147 to 182. The SEMLF "formal" error in the ΔV = 160 km s^{-1} case is only $\sim$ 2 times larger than in the ΔV = 60 km s^{-1} case, but the $\hat{\chi}^2$ – weighted error is ~23 times larger.

We note a similar trend for the spectral components with a larger flux ratio (4:1) in Fig. 5a (ΔV = 60 km s^{-1}) to Fig. 5b (ΔV = 160 km s^{-1}), except that both techniques fit close to the velocity of the brighter peak (4720 km s^{-1}). In Fig. 5b, SEMLF primarily fits the brighter peak, and the secondary peak, which does displace the resulting line profile, is not strongly reflected in the unweighted error. On the other hand, the XC error and the SEMLF weighted error are ~5 and 6 times larger, respectively, than the errors in Fig. 5a, indicating model mismatch. Again, r decreases substantially from 164 to 29; ω stays roughly the same.

Figs. 6 – 8 explore these trends for a range of ΔV. The model velocity components have flux ratios of 4:3, 2:1 or 4:1; the brighter component is always at the larger velocity. The model spectra for each component are identical to the spectra above (e.g. Fig. 5b provides the points with ΔV = 160 km s^{-1} and flux ratio 4:1 for Figs. 6 – 8).

To explore the effects of lesser peaks on the derived velocity for the two techniques, we compare XC and SEMLF results to the velocity of the brightest component. Fig. 6 shows the difference between the velocity determined by each technique and the input model velocity of the brighter component, as a function of ΔV. We compare the results to the flux-weighted mean of the Hα peaks (thin dotted line). The solid line shows the XC results; the dashed line shows the SEMLF results. For small ΔV, the XC line is close to or above the SEMLF line — the XC velocity is generally closer to the velocity of the brighter component and SEMLF tracks the flux-weighted mean. At larger ΔV, in models with larger component flux ratios, the lines cross — SEMLF stops tracking the flux-weighted mean and the SEMLF result is closer to the velocity of the bright component. In the 4:3 flux ratio model, SEMLF switches to fitting only the brighter peak at $\Delta V \geq 280$ km s^{-1} (not shown); in this model, the greatest difference between the velocities from the two techniques is 44% of the component separation, when ΔV = 240 km s^{-1} = 2.3 times the FWHM of Hα. In summary, at low component separation, for all the models, SEMLF fits closer to the mean of the components, while XC fits closer to the brightest peak. At larger component separation, when the component flux ratio is large, this trend reverses and SEMLF fits the brighter peak only.

Fig. 7 shows the errors computed by each technique as a function of component velocity separation, for XC (solid line) and SEMLF (dashed line — unweighted; dotted line — weighted by $\hat{\chi}^2$). These figures illustrate the necessity of weighting the formal SEMLF errors by $\hat{\chi}^2$. The XC errors and the weighted SEMLF errors increase dramatically as ΔV increases, indicating the presence of additional components, although the weighted SEMLF errors begin to decrease again at very large ΔV, for 2:1 or 4:1 flux ratios, when only the strongest peaks enter the fit. In this case, the $\hat{\chi}^2$ remains large, as shown in the next figure.

In Fig. 8a and b, we illustrate the behavior of the XC errors and of the $\hat{\chi}^2$ of the SEMLF Gaussian fits for flux ratios of 4:3 and 4:1; we plot the r value on top, then ω, then $\hat{\chi}^2$. In the 4:1 flux ratio model ω increases until ΔV is so large that only one component contributes to the fit and ω begins to decrease. However, r decreases with ΔV for each model at large ΔV, signaling the increasing inadequacy of a single-component template as the velocity components separate. The decrease in r accounts for the increase in the errors; thus the errors increase monotonically as ΔV increases. Likewise, $\hat{\chi}^2$ increases rapidly as ΔV increases, slowing only at the very largest ΔV, where the component ratio is 4:1.

In these examples, XC and SEMLF compute velocities which differ by up to 44 % of the component velocity separation. XC errors increase monotonically, and by a large factor, as the velocity component separation (ΔV) increases. For larger component flux ratios, the unweighted SEMLF errors remain small and begin to decrease at large ΔV, making them unsuitable for spectra with multiple velocity components. The $\hat{\chi}^2$ – weighted SEMLF errors behave much more like the XC errors, increasing by large factors as ΔV increases, although they do not increase monotonically for large component flux ratios with large ΔV. Note that because the $\hat{\chi}^2$ taken alone does increase monotonically, $\hat{\chi}^2$ is preferable to the weighted error as an indicator of multiple velocity components when using SEMLF.

The cross-correlation technique flags the multiple-component case consistently, even as the secondary component becomes weak or widely separated in velocity from the primary component. Cross-correlation errors are less model-dependent than formal χ^2-minimization errors in the sense that they include mismatch between the model (the template) and the spectrum. Thus in spite of a template-dependent systematic bias in the errors, the cross-correlation errors roughly scale properly; they even reflect velocity components that do not overlap the strongest component in wavelength. The $\hat{\chi}^2$ of the SEMLF technique also reflects the presence of secondary velocity components that overlap the main component in wavelength.

4. Two-Dimensional Model Rotation Curves

Here, we model effects from multiple velocity components that can be important in longslit galaxy spectroscopy. We compare the results of XC and SEMLF.

4.1. Non-Gaussian Profiles

When neighboring discrete disk components of a galaxy are not sufficiently resolved, they overlap spatially, resulting in spectra with multiple velocity components. Spectra with multiple velocity components also occur when galaxies have kinematically distinct, cospatial components, like circumnuclear disks. We illustrate these two cases with two-dimensional models of "rotation curves"; we construct the models using artificial one-dimensional emission-line templates, or sums of templates, created with **linespec** in RVSAO, joined with **mk1dspec** and **mk2dspec** in NRAO.ARTDATA.

Fig. 9 is an image of a model spectrum which illustrates spatially overlapping components. Fig. 9a shows a greyscale plot of the region around Hα of the model longslit spectrum — the dispersion axis is horizontal, while the spatial axis is vertical and spans 100 pixels. Our two-dimensional spectra consist of segments (the lumps in the image) with Gaussian intensity variations in the spatial direction. The horizontal lines in the top portion of Fig. 9b show each segment as a horizontal line across its spatial FWHM, where the spatial direction is along the x-axis. The actual "emission" extends beyond its FWHM. The y-axis shows the velocity of each segment. The circles show the results from XC (left) and SEMLF (right), with the errors on an expanded scale at the bottom of the figure. We show both unweighted SEMLF errors and SEMLF errors weighted by $\hat{\chi}^2$.

The velocity structure is Gaussian and does not vary along each segment; line profiles are irregular (e.g. double-peaked) where the segments overlap and thus more than one segment contributes to the spectrum. Widths in the dispersion direction are fixed by the basic spectrum, Fig. 1, used in the models. As in the one dimensional case, we add read noise (7.0 e^-) and Poisson noise to the spectra using **mknoise** in NRAO.ARTDATA. Although the model is a step function in velocity, the calculated rotation curve varies smoothly because the segments at different velocities overlap spatially.

The biggest differences between the XC and SEMLF curves occur between segments, at pixel $\sim$55. The errors behave similarly for the two techniques. The errors for both models increase significantly in the overlap regions; they are larger where adjacent components are separated by larger velocities. The weighted SEMLF errors increase by a larger factor than the unweighted errors increase. As expected, ω increases in the regions of overlap, and r decreases; r also decreases when the signal fades (e.g. at pixel values > 95).

The model in Fig. 10a resembles a 2-component galaxy with an inner disk (see e.g. Rubin et al. 1997). Fig. 10b shows the positions and velocities of the segments; each segment has a FWHM of 4 pixels in the spatial direction, although we plot only points. The outer disk model (dashed line) approximately traces a standard rotation curve. The second model component (thick solid line) represents an inner gas disk; it rotates as a solid body, is twice as intense as the outer curve, and has emission lines twice as broad.

Fig. 10b shows that the techniques fit similar rotation curves, with similar errors, to the model. In the cross-correlation case, the $\frac{1}{1+r}$ contribution to the error decreases in the center of the model due to larger signal, but *the cross-correlation errors increase* because ω increases, signaling the presence of the second, distinct velocity component (see Fig. 10b).

When the formal SEMLF errors are not weighted by $\hat{\chi}^2$, *the errors decrease in the center of the model* due to the larger S/N ratio. Only $\hat{\chi}^2$–weighted errors reflect the velocity uncertainty due to the two components, because $\hat{\chi}^2$ increases as a single Gaussian becomes a poor fit.

4.2. Nonstandard Line Ratios with Non-Gaussian Profiles

Nonstandard line ratios (e.g. in the nuclear regions of AGN) are another potential source of template or model mismatch. In real galaxies, non-thermal activity and multiple components often arise together; we consider a combined model here. We compare the XC and SEMLF responses to nonstandard line ratios in the nuclear region using the "inner disk" model; we plot results in Fig. 11. The left column of Fig. 11 shows the model of Fig. 10 on top, the XC velocity minus the SEMLF velocity in the middle, and the errors from the two techniques on the bottom. The middle column model has [NII] lines with heights greater by a factor of ten in the inner disk component; the outer disk and the [SII] and Hα lines remain the same. The model we show in the right column has [NII] lines that are ten times larger and no Hα emission in the inner disk component. Again, the outer disk and [SII] profiles remain the same — thus, there is a small amount of Hα emission from the outer disk component. The velocity structure of the models remains the same.

The changing line ratios influence the results of the techniques somewhat, especially at the edge of the inner disk component. The peak difference between SEMLF and XC results occurs at aperture 40 in Fig. 11e, where the difference is 60 km s^{-1}, corresponding to 52% of the velocity difference between the inner and outer disks at that aperture. In XC, the contributions to the velocity from each emission line are effectively weighted by their heights in the template. Hα is the strongest emission line in the HII region template we use. Thus, XC weights the contribution of the faint outer disk much more heavily than SEMLF does, due to its small amount of Hα emission. Peak heights in SEMLF may vary to accommodate changing line ratios; thus the SEMLF errors increase only moderately. The XC errors increase due to spectrum/template mismatch. When the mismatch is severe, the templates can be adjusted. For example, when Balmer absorption eliminates Hα, the line can be removed from the template.

Increased errors may result from many sources, including changing line ratios, lower S/N, or additional velocity components. All three of these effects increase the r error statistic in XC. ω reflects multiple velocity components that are not spaced too widely. To determine the cause of increased errors, it is usually necessary to examine the line profiles in the region of interest. However, the dip in the computed rotation curve at the transition between the inner and outer disk (Fig. 10, aperture 43), accompanied by the increased error, or especially by an increased ω, provides a strong clue to the nature of the increase — a second velocity component. In automated reduction with XC, one can select out rotation curves where there are many adjacent points with large errors as candidates for multiple-component systems. With SEMLF, the formal errors do not clearly reflect additional components; they flag only regions of low S/N ratio. The effects of spectrum/model mismatch are isolated by $\hat{\chi}^2$; regions with multiple velocity components can be flagged as regions where $\hat{\chi}^2$ is significantly greater than 1.

5. Application of XC to Real Galaxies

Barton et al. (1999) use XC to reduce a large sample of rotation curves of galaxies in pairs; Fig. 12a shows an example. Barton et al. (1999) describe the reduction procedures in detail. The curve shows the inner part of CGCG 373-046, which has a separate kinematic component in the center. The errors enlarge in the center to reflect this component. Fig. 12b shows Hα and [NII] line profiles at various slit positions; the line profiles are clearly doubled near the center of the galaxy, where the errors enlarge.

The models described in this paper explore only the simplest cases; they exclude the effects of uncertainty in wavelength solution, night sky contamination, cosmic rays, non-Gaussian line profiles other than multiple-component profiles, continuum emission and extra emission lines (that are not included in the template spectra). At minimum, the steps necessary for longslit redshift reduction are: (1) bias subtraction and flat-fielding, (2) "line-straightening," or solving for the wavelength solution at each pixel in the spatial direction, (3) cosmic-ray removal and sky subtraction, (4) a correction for differential atmospheric refraction and (5) a redshift determination at each point along the slit.

Template selection or construction is also necessary, after step (4), when cross-correlation is used in step (5). The best template will reflect the spectrum of a typical single-velocity component. Barton et al. (1999) build cross-correlation templates using the observed relative line heights and widths. To measure line heights and widths for the template, they run the task **emsao** in the RVSAO package (Kurtz & Mink 1998) which fits unconstrained Gaussian functions to the major emission lines with enough signal. They use each aperture in which **emsao** finds all 5 emission lines; they compute the median relative line heights and the median absolute line widths for each run (4 – 5 nights). Barton et al. use the resulting values as input parameters to create a template of smooth Gaussian "emission" lines with **linespec** in RVSAO. They test the performance of separate templates for each observing run, night, and galaxy and find that a run template yields the smallest errors on average. In practice, a single, carefully constructed template used for all data from a particular instrumental setup should suffice for most purposes (see Kurtz & Mink 1998).

For the low S/N case, a small amount of fine-tuning is necessary to extract complete rotation curves; Barton et al. find that restricting the wavelength range of allowable solutions to within

$\sim$1000 km s^{-1} of the systemic velocity is easy to implement and yields accurate curves in low S/N regions, although it may exclude extreme cases of separate velocity components. For example, Morris et al. (1985) find a component of NGC 7582 1300 km s^{-1} off the systemic velocity. .

6. Conclusion

We describe the use of cross-correlation to determine velocity fields of nearby galaxies using optical emission lines observed with longslit spectroscopy. The method is easily automated, makes simultaneous use of the strongest emission lines, and is efficient for low signal-to-noise spectra. As we describe, the technique yields well-defined errors.

We compare cross-correlation to a fundamentally different, parametric technique, simultaneous Gaussian fitting of emission lines. Velocities and errors computed by the two techniques agree very well in the case of a single Gaussian velocity component.

When line profiles are non-Gaussian (e.g. because more than one component contributes at the same slit position), the results of the two techniques differ. In our examples, the XC and SEMLF techniques give velocities which differ by up to 52% of the component velocity separation. For standard HII region emission line ratios and component separations up to 1.5 times the FWHM of Hα, XC fits closer to the brightest peak and SEMLF fits closer to the mean. As the separation becomes larger, SEMLF also switches to the brightest peak.

The formal SEMLF error and the error computed by XC differ significantly because the XC error consistently reflects mismatch of the spectrum and model (template), whereas formal SEMLF errors are model-dependent. However, when SEMLF errors are weighted by $\hat{\chi}^2$, SEMLF errors behave much more like XC errors. Only minor differences remain, as the SEMLF errors do not increase monotonically in reflecting components with increasing velocity separation from the primary velocity component. Thus, the $\hat{\chi}^2$-weighting procedure is empirically justified by comparison with XC.

For automated reduction of large data sets, multiple components and other non-Gaussian line structures can be flagged for further inspection using the increase in either the XC error (or the statistic ω), or the SEMLF $\hat{\chi}^2$. However, a complete description of these multiple-component cases *requires additional modeling* to explore the different components.

The choice of whether to use XC or SEMLF should be guided by the following considerations: (1) XC is readily available as the IRAF routine **xcsao**, in the RVSAO package. It is easily automated and requires no initial redshift guess (although constraints on the allowed solutions are useful for spectra with small S/N ratios), (2) for two-component profiles, XC generally fits closer to the brighter peak, whereas SEMLF shifts from fitting the flux-weighted mean to fitting the brighter peak for larve ΔV and large flux ratios, (3) both XC errors and the SEMLF $\hat{\chi}^2$ statistic may be used to flag multiple components, (4) the XC error increases monotonically with peak velocity separation, as does the SEMLF $\hat{\chi}^2$, but the SEMLF errors do not behave monotonically because at large ΔV, SEMLF switches to fitting only the brightest peak, (5) SEMLF errors are exact in the ideal Gaussian case, whereas the overall normalization of the XC errors must be calibrated for each template if $\pm 20\%$ errors are not accurate enough, (6) in XC the choice of template fixes the model emission line ratios and linewidths, whereas these can vary (or be fit), in SEMLF, and (7) SEMLF measures shape information for the line profiles in the single-Gaussian case.

We thank D. Fabricant, D. Mink and S. Tokarz for useful discussions and assistance with the software. E. B. and S. K. received support from Harvard Merit Fellowships. E. B. received support from a National Science Foundation Graduate Research Fellowship, and S. K. received support from a NASA Graduate Student Researchers Program Fellowship. This research was supported in part by the Smithsonian Institution.

REFERENCES

Babcock, H. W. 1939, Lick Obs. Bull., no. 19, 41

Barton, E. J., et al. 1999, in preparation

Bureau, M., & Freeman, K. C. 1999, AJ, 118, 126

Burbidge, E. M., & Burbidge, G. R. 1975, in Stars and Stellar Systems, Vol. 4, Galaxies and the Universe, ed. A. Sandage, M. Sandage, & J. Kristian (Chicago Univ. Chicago Press) 81

Courteau, S. 1997, AJ, 114, 2402

Franx, M., Illingworth, G., & Heckman, T. 1989, ApJ, 344, 613

Kannappan, S. J., et al. 1999, in preparation

Keel, W. C. 1996, ApJ, 106, 27

Kurtz, M. J., & Mink, D. J. 1998, PASP, 110, 934

Landsman, W. B. 1995, in Astronomical Data and Analysis Software and Systems IV, ASP Conference Series, Vol. 77, R.A. Shaw, H.E. Payne, and J.JE. Hayes, eds., p. 437

Marziani, P., Keel, W. C., Dultzin-Hacyan, D., & Sulentic, J. W. 1994, ApJ, 435, 668

Mathewson, D. S., Ford, V. L., & Buchhorn, M. 1992, ApJS, 81, 413

Márquez, I., & Moles, M. 1996, A&A, 120, 1

Merrifield, M. R., & Kuijken, K. 1994, ApJ, 432, 575

Morris, S., Ward, M., Whittle, M., Wilson, A. S., & Taylor, K. 1985, MNRAS, 216, 193

Osterbrock, D. E. 1989, Astrophysics of Gaseous Nebulae and Active Galactic Nuclei (Mill Valley: University Science Books)

Pease, F. G. 1918, Proc. Natl. Acad. Sci., 4, 21

Press, W. H., Teukolsky, S. A., Vetterling, W. T., & Flannery, B. P. 1992, Numerical Recipes in C, Second Edition (Cambridge: Cambridge Univ. Press)

Rix, H.-W., & White, S. D. M. 1992, MNRAS, 254, 389

Rubin, V. C., Burstein, D., Ford, W. K., Jr., & Thonnard, N. 1985, ApJ, 289, 81

Rubin, V. C. 1995, ApJ, 451, 419

Rubin, V. C., Kenney, J. D. P., & Young, J. S. 1997, AJ, 113, 1250

Tody, D. 1986, in Proc. SPIE Instrumentation in Astronomy VI, ed. D. L. Crawford, 627, 733

Tody, D. 1993, in Astronomical Data Analysis Software and Systems II, A.S.P. Conference Series, Vol. 52, eds. R. J. Hanisch, R. J. V. Brissenden, and J. Barnes, 173

Tonry, J. L., & Davis, M. 1979, AJ, 43, 393 (TD)

van der Marel, R. P., & Franx, M. 1993, ApJ, 407, 525

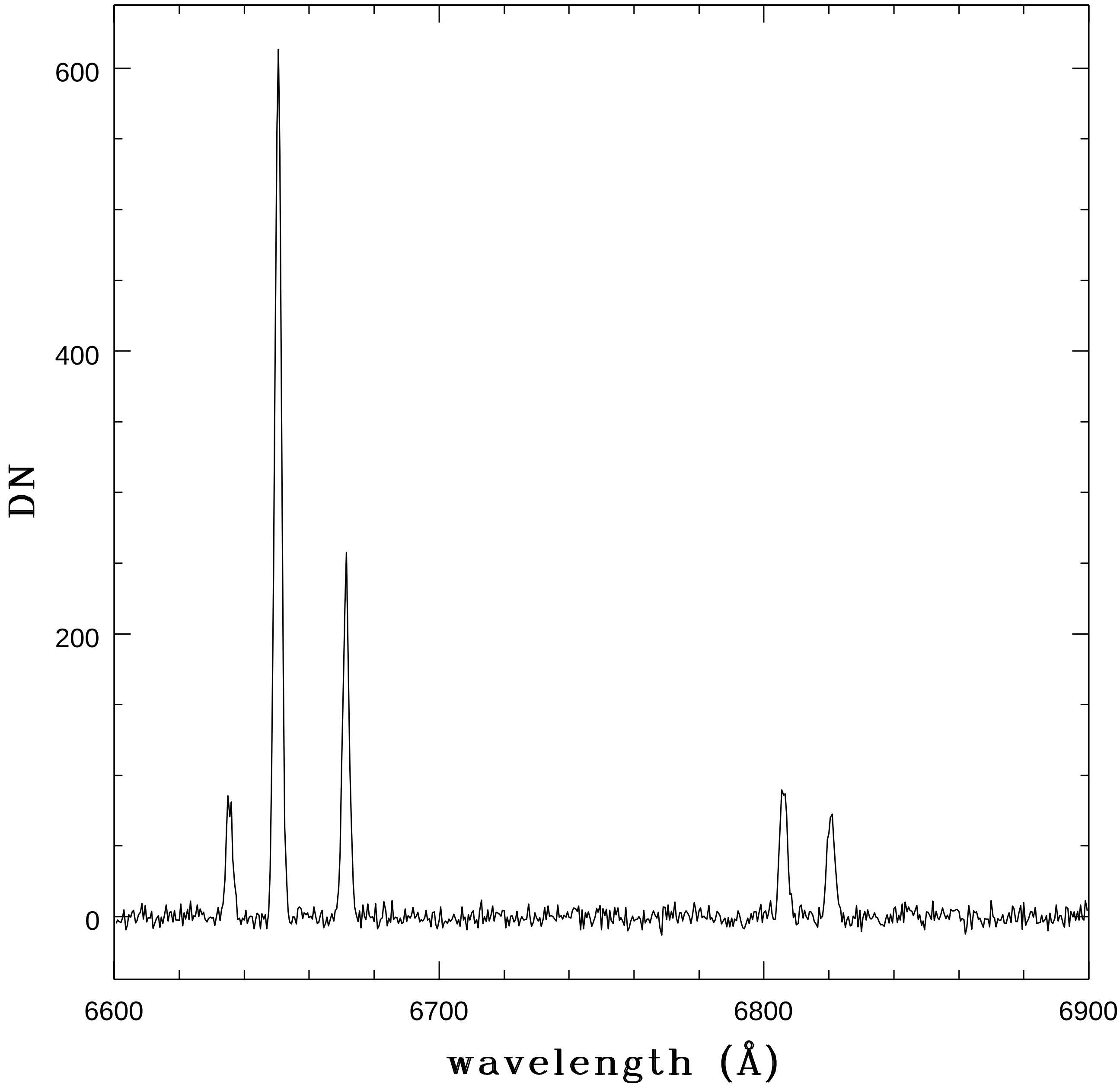

Fig. 1.— The basic model spectrum, shifted to 4000 km s^{-1}.

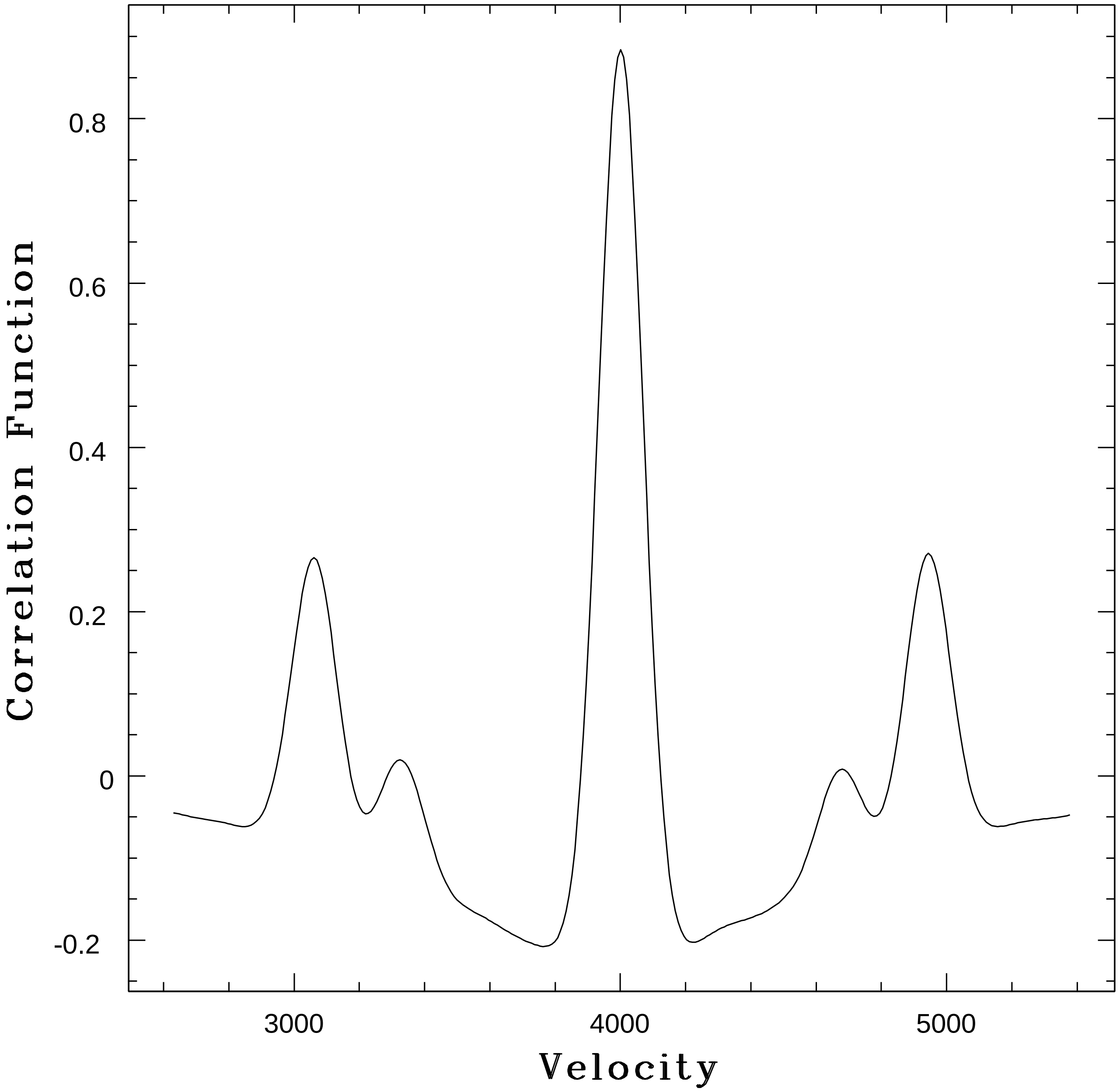

Fig. 2.— The correlation peak of the large signal-to-noise spectrum in Fig. 1, fit by **xcsao** to determine the XC velocity.

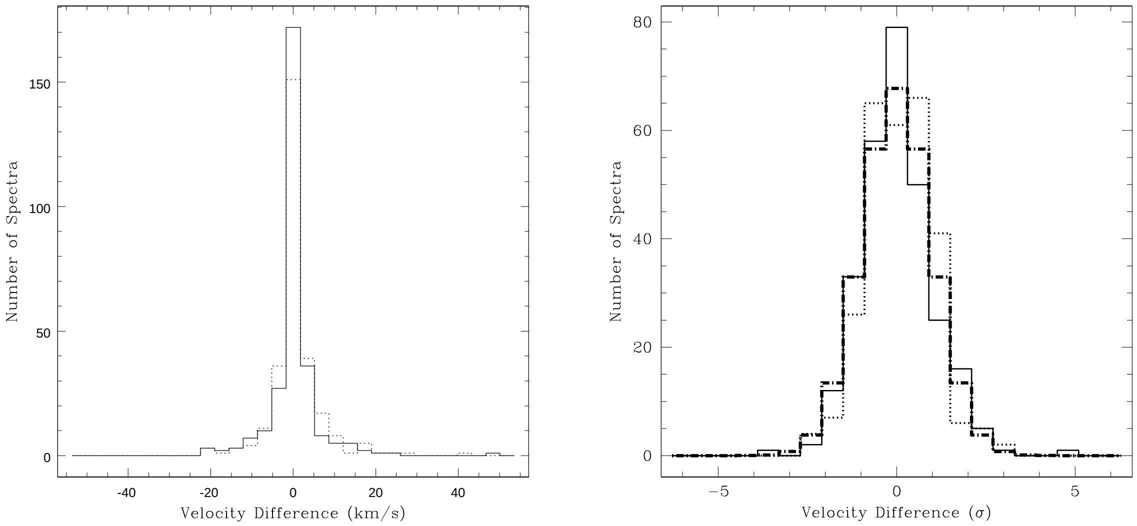

Fig. 3.— 283 Gaussian spectra at different noise levels: (a) histogram of the difference between the true velocity and the XC velocity (solid line), and the true velocity and the SEMLF velocity (dotted line) in km/s and, (b) histogram of the difference between the true velocity and the XC velocity divided by the XC error (solid line), or the true velocity and the SEMLF velocity divided by the $\hat{\chi}^2$-weighted SEMLF error (dotted line). The thick dot-dashed line is a Gaussian distribution with $\sigma = 1$.

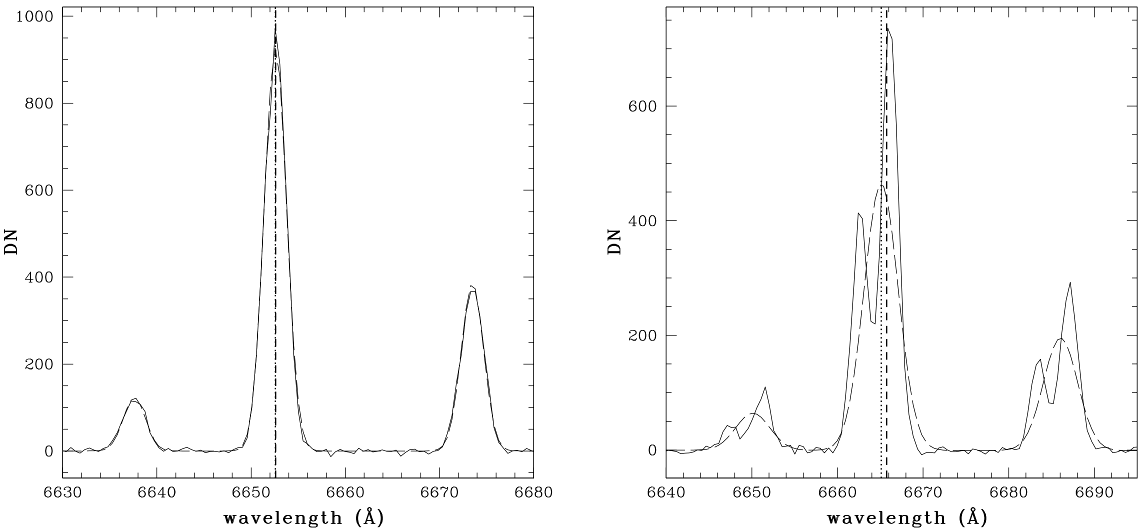

Fig. 4.— Two-component spectra with small and large component velocity separations, ΔV. The component flux ratio is 2:1. Each figure shows the spectrum (solid line) with SEMLF fit (dot-dashed line) and, XC (vertical dashed line) and SEMLF (vertical dotted line) results. (a) $\Delta V = 60$ km s^{-1} $= 0.58$ FWHM$_{\mathrm{H}\alpha}$, where FWHM$_{\mathrm{H}\alpha}$ is the FWHM of the Hα line. The brighter component is at 4120 km s^{-1}. The XC and SEMLF results overlap; they are 4101.2 ± 0.3 and $4100.8 \pm 0.3(\pm 0.5)$ km/s, respectively, where the second SEMLF error is weighted by $\hat{\chi}^2$. (b) $\Delta V = 160$ km s^{-1} $= 1.5$ FWHM$_{\mathrm{H}\alpha}$. The brighter component is at 4720 km s^{-1}; the XC and SEMLF results are 4701.3 ± 4.6 and $4672.8 \pm 0.7(\pm 10.9)$ km/s.

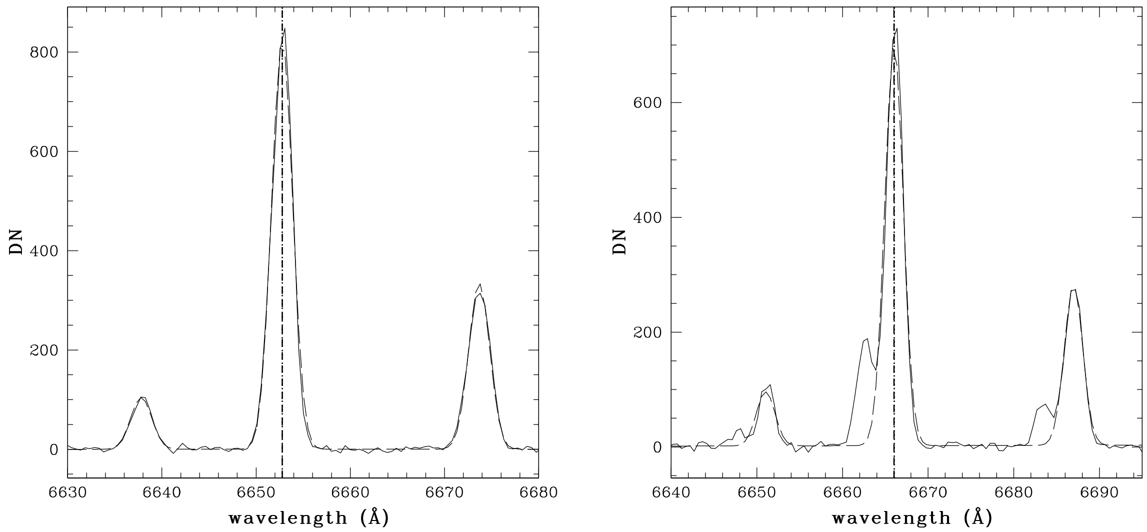

Fig. 5.— Two-component spectra. The component flux ratio is 4:1; the figure shows the spectrum (solid line) with the SEMLF fit (dot-dashed line) and, XC (vertical dashed line) and SEMLF (vertical dotted line) results. The component velocity separations are (a) ΔV = 60 km s^{-1} = 0.58 FWHM$_{\mathrm{H}\alpha}$, where FWHM$_{\mathrm{H}\alpha}$ is the standard deviation of the Hα line. The brighter component is at 4120 km s^{-1}. The XC and SEMLF results overlap; they are 4109.6 ± 0.3 and $4109.3 \pm 0.3(\pm 0.5)$ km/s respectively, where the second SEMLF error is weighted by $\hat{\chi}^2$, and (b) $\Delta V = 160$ km s^{-1} = 1.5FWHM$_{\mathrm{H}\alpha}$. The brighter component is at 4720 km s^{-1}; the XC and SEMLF results are 4714.0 ± 1.8 and $4715.0 \pm 0.4(\pm 3.0)$ km/s.

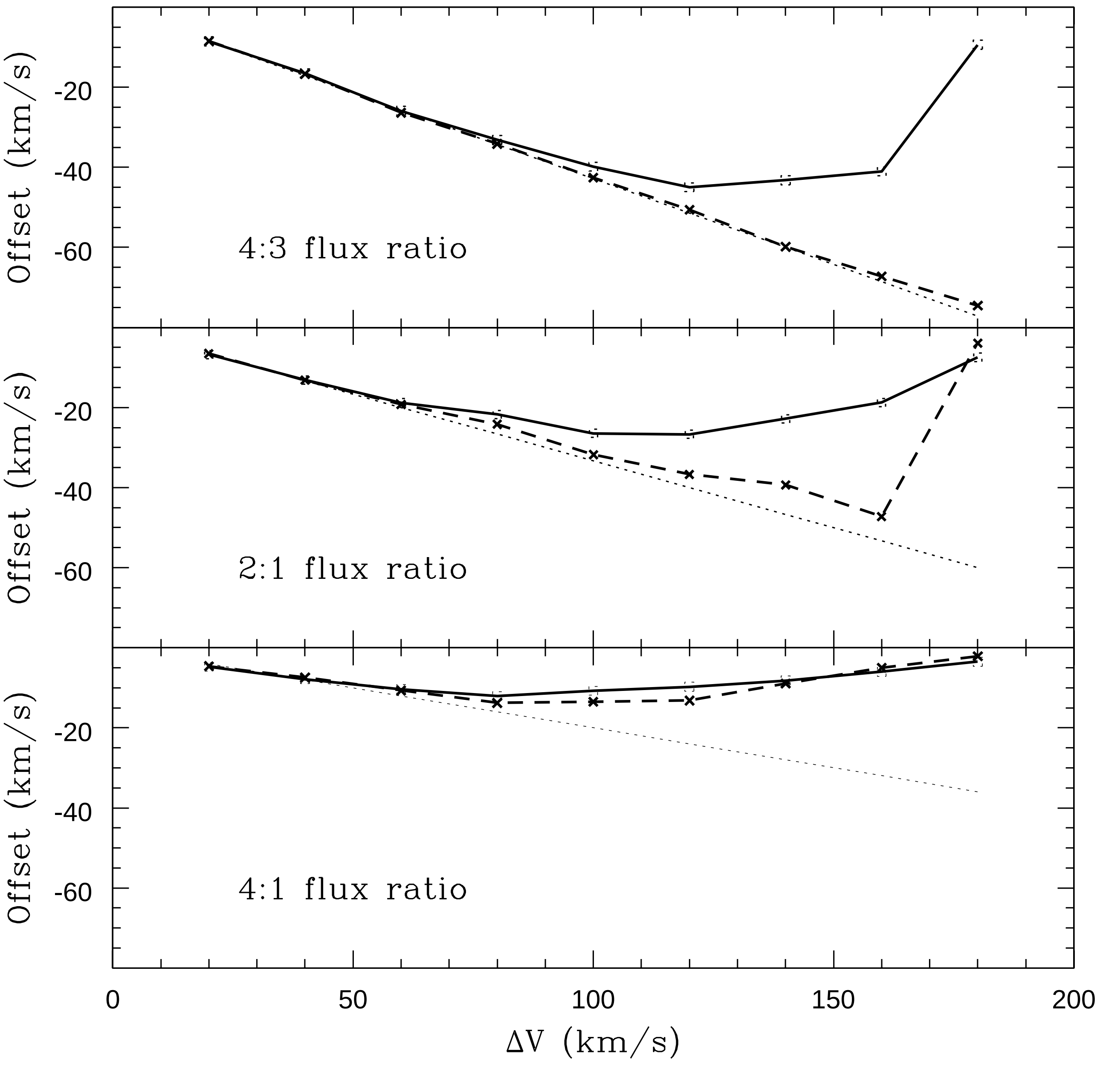

Fig. 6.— Velocity offsets as a function of velocity component separation from two-component spectra for XC (solid line) and SEMLF (dashed line). The velocity offset is equal to the velocity solution minus the true velocity of brightest component in the model. The thin dotted line is the flux-weighted mean of the two components. The flux ratios are 4:3 (top), 2:1 (middle), and 4:1 (bottom). For different spectral resolutions, ΔV must be scaled by 104 km s^{-1}/FWHM, where FWHM is for the the Hα line.

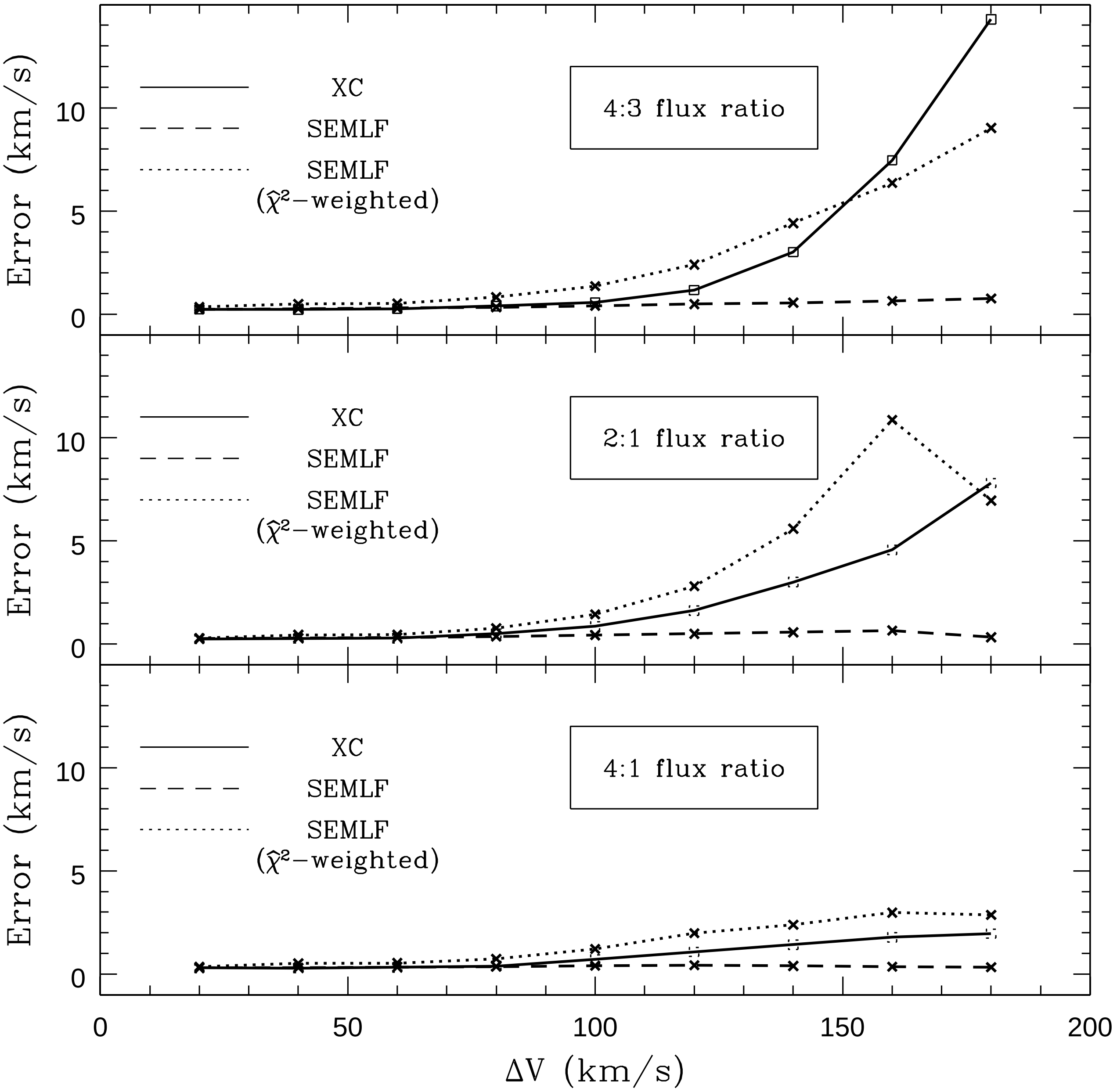

Fig. 7.— Velocity errors as a function of velocity component separation for XC (solid line) and SEMLF (dashed line). As in Fig. 6, the flux ratios are 4:3 (top), 2:1 (middle), and 4:1 (bottom).

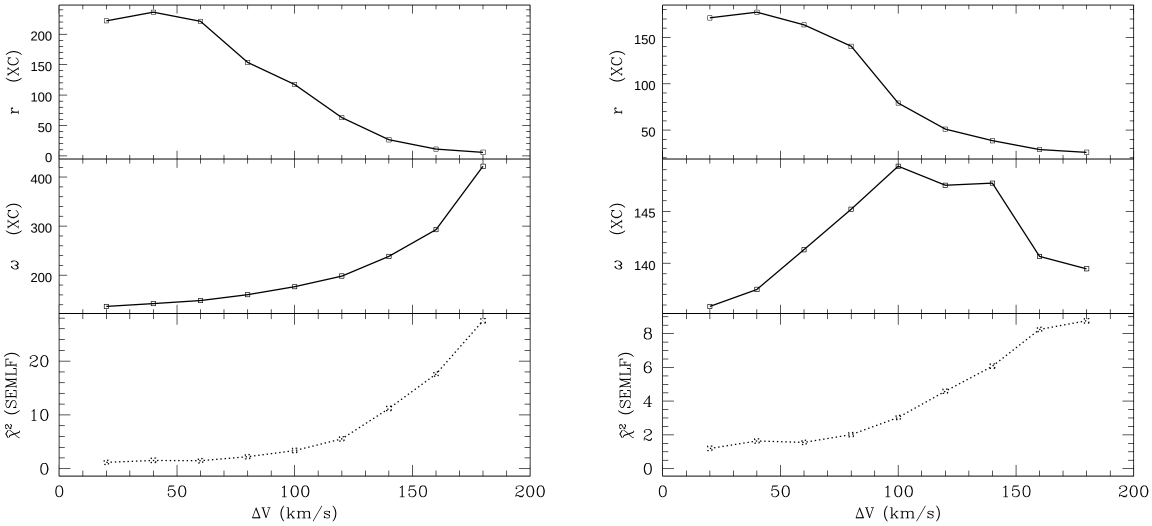

Fig. 8.— Error contributions: r, ω and $\hat{\chi}^2$ as a function of velocity component separation, ΔV, for (a) the 4:3 flux ratio and (b) the 4:1 flux ratio. We omit the 2:1 flux ratio case, which looks qualitatively similar to (b).

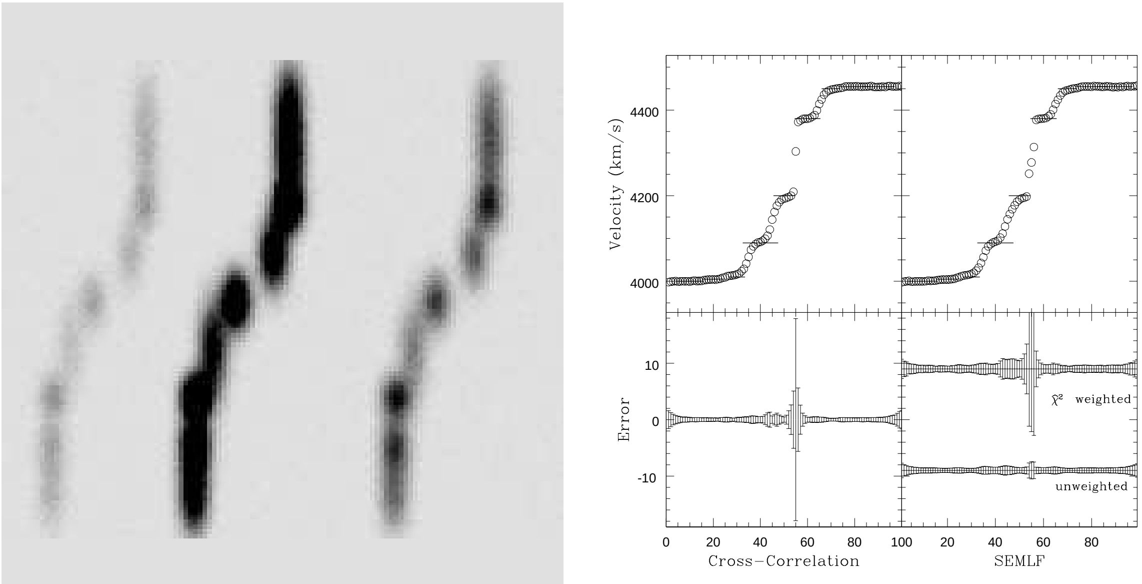

Fig. 9.— "Overlapping segment" spectral model: (a) greyscale image, showing the model Hα and Nitrogen lines; the dispersion axis is in the vertical direction and the spatial axis is horizontal and, (b) results and errors for XC and SEMLF. The top portion of (b) shows the rotation curves superimposed on the model flux components (solid horizontal lines), and the bottom portion shows the error bars on an enlarged scale, including both weighted and unweighted SEMLF errors. The left sides of the rotation curves in (b) corresponds to the bottom of (a).

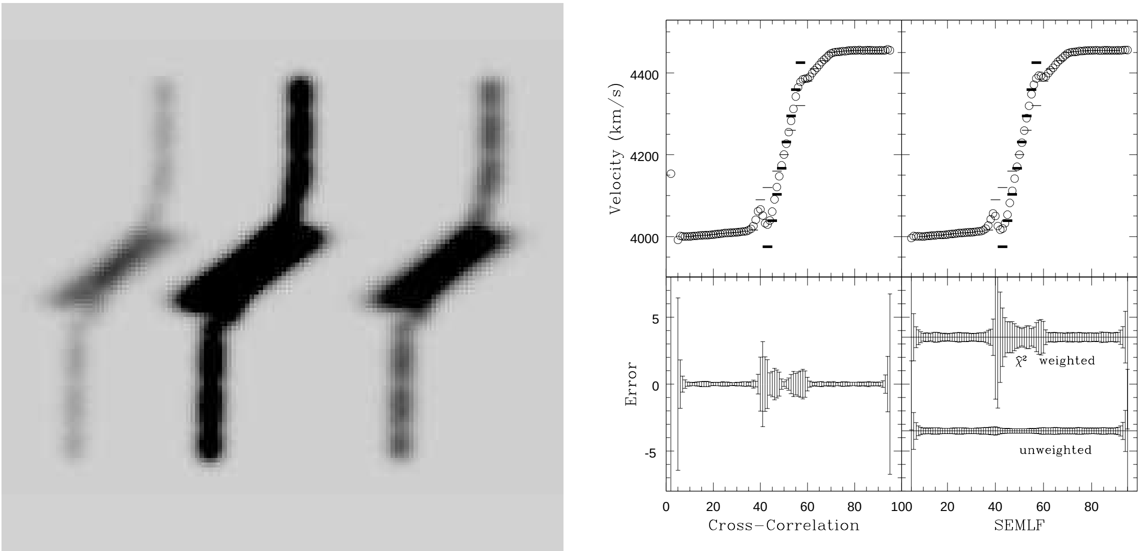

Fig. 10.— “Inner disk” spectral model (see Fig. 9 for a description of the figure, but note the different error scale here). Note that the XC and weighted SEMLF errors increase in the center, reflecting the two kinematic components, but the (formal) unweighted SEMLF errors decrease in the center — they fail to reflect the complex velocity structure.

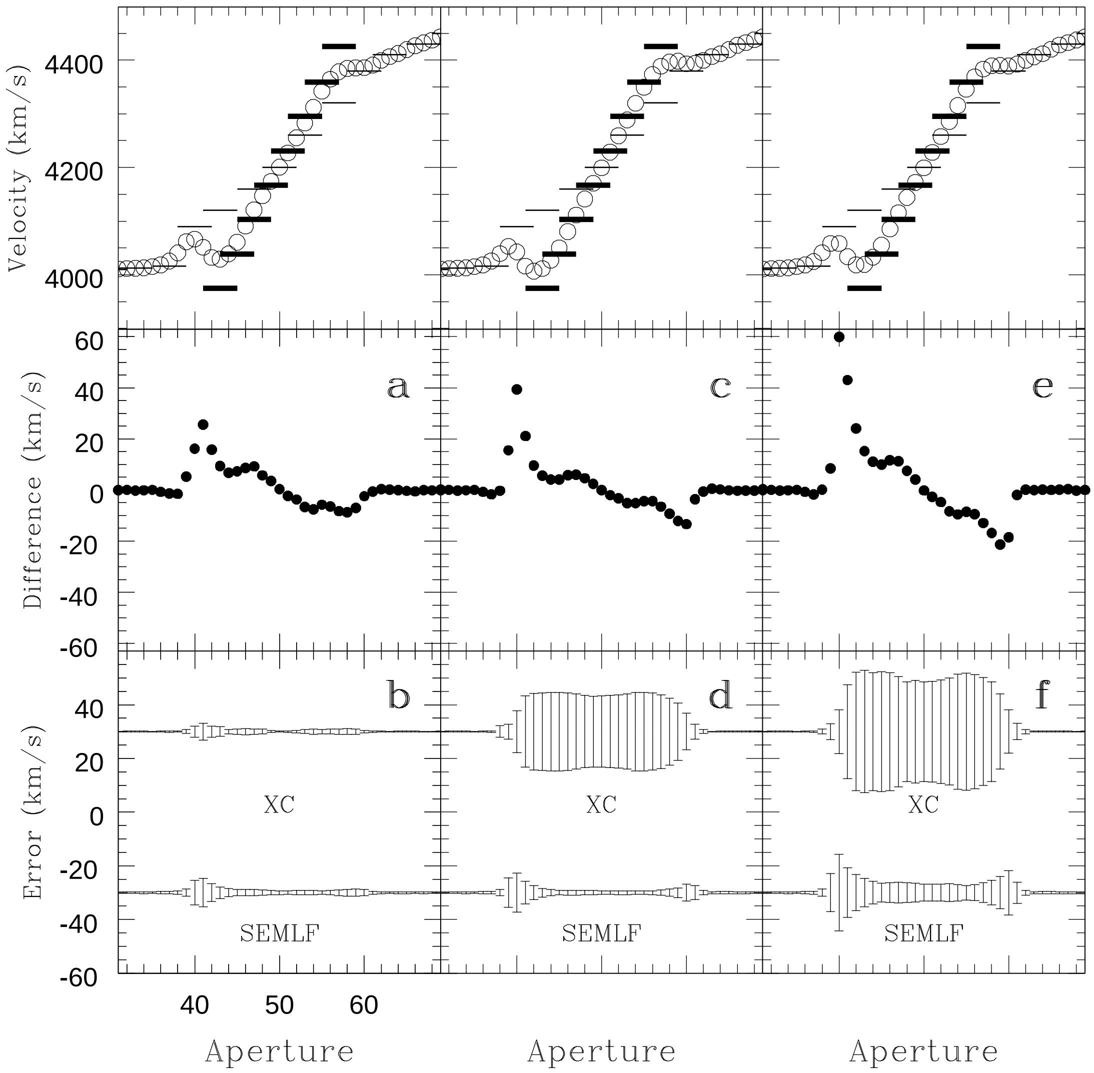

Fig. 11.— XC and SEMLF velocity differences and errors for the "inner disk" model and models with varying line ratios for the inner disk component. The top figures are the XC rotation curves. The middle figures are the SEMLF velocity minus the XC velocity; the bottom figures are errors for each technique. (a) and (b) are the "inner disk" model from Fig. 10. (c) and (d) are the same model, except the [NII] line heights are increased by a factor of 10 for the wide inner disk velocity component. (e) and (f) also have [NII] heights increased by a factor of 10, and no Hα emission from the inner disk component.

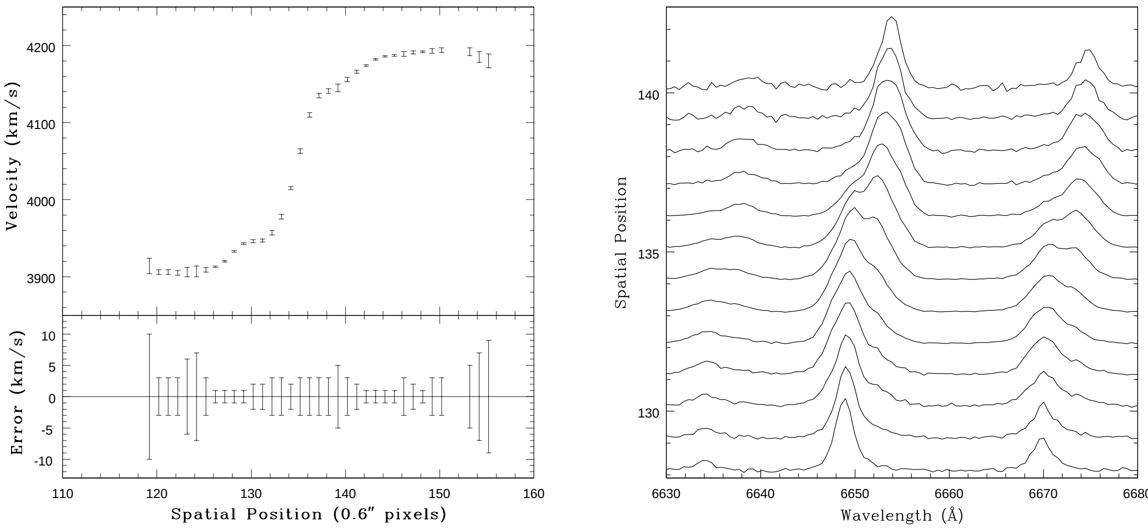

Fig. 12.— The inner rotation curve of a real galaxy with a separate kinematic component in its center: (a) XC rotation curve and errors, and (b) Nitrogen and Hα line profiles at spatial positions near the center of the galaxy. Each profile is normalized for display purposes — the true emission lines have more flux in the center than on the outskirts. The labels on the y axis correspond to the values on the x axis of (a).